

Forward π^0 Production and Associated Transverse Energy Flow in Deep-Inelastic Scattering at HERA

H1 Collaboration

Abstract

Deep-inelastic positron-proton interactions at low values of Bjorken- x down to $x \approx 4 \cdot 10^{-5}$ which give rise to high transverse momentum π^0 -mesons are studied with the H1 experiment at HERA. The inclusive cross section for π^0 -mesons produced at small angles with respect to the proton remnant (the forward region) is presented as a function of the transverse momentum and energy of the π^0 and of the four-momentum transfer Q^2 and Bjorken- x . Measurements are also presented of the transverse energy flow in events containing a forward π^0 -meson. Hadronic final state calculations based on QCD models implementing different parton evolution schemes are confronted with the data.

To be submitted to Eur. Phys. J. C

A. Aktas¹⁰, V. Andreev²⁴, T. Anthonis⁴, A. Asmone³¹, A. Astvatsatourov³⁵, A. Babaev²³,
 S. Backovic³⁵, J. Bähr³⁵, P. Baranov²⁴, E. Barrelet²⁸, W. Bartel¹⁰, S. Baumgartner³⁶,
 J. Becker³⁷, M. Beckingham²¹, A. Beglarian³⁴, O. Behnke¹³, O. Behrendt⁷, A. Belousov²⁴,
 Ch. Berger¹, T. Berndt¹⁴, J.C. Bizot²⁶, J. Böhme¹⁰, M.-O. Boenig⁷, V. Boudry²⁷, J. Bracinik²⁵,
 W. Braunschweig¹, V. Brisson²⁶, H.-B. Bröker², D.P. Brown¹⁰, D. Bruncko¹⁶, F.W. Büsser¹¹,
 A. Bunyatyan^{12,34}, A. Burrage¹⁸, G. Buschhorn²⁵, L. Bystritskaya²³, A.J. Campbell¹⁰,
 S. Caron¹, F. Cassol-Brunner²², V. Chekelian²⁵, D. Clarke⁵, C. Collard⁴, J.G. Contreras^{7,41},
 Y.R. Coppens³, J.A. Coughlan⁵, M.-C. Cousinou²², B.E. Cox²¹, G. Cozzika⁹, J. Cvach²⁹,
 J.B. Dainton¹⁸, W.D. Dau¹⁵, K. Daum^{33,39}, M. Davidsson²⁰, B. Delcourt²⁶, N. Delerue²²,
 R. Demirchyan³⁴, A. De Roeck^{10,43}, E.A. De Wolf⁴, C. Diaconu²², J. Dingfelder¹³, P. Dixon¹⁹,
 V. Dodonov¹², J.D. Dowell³, A. Dubak²⁵, C. Duprel², G. Eckerlin¹⁰, V. Efremenko²³, S. Egli³²,
 R. Eichler³², F. Eisele¹³, M. Ellerbrock¹³, E. Elsen¹⁰, M. Erdmann^{10,40,e}, W. Erdmann³⁶,
 P.J.W. Faulkner³, L. Favart⁴, A. Fedotov²³, R. Felst¹⁰, J. Ferencei¹⁰, S. Ferron²⁷,
 M. Fleischer¹⁰, P. Fleischmann¹⁰, Y.H. Fleming³, G. Flucke¹⁰, G. Flügge², A. Fomenko²⁴,
 I. Foresti³⁷, J. Formánek³⁰, G. Franke¹⁰, G. Frising¹, E. Gabathuler¹⁸, K. Gabathuler³²,
 J. Garvey³, J. Gassner³², J. Gayler¹⁰, R. Gerhards^{10†}, C. Gerlich¹³, S. Ghazaryan³⁴,
 L. Goerlich⁶, N. Gogitidze²⁴, S. Gorbounov³⁵, C. Grab³⁶, V. Grabski³⁴, H. Grässler²,
 T. Greenshaw¹⁸, G. Grindhammer²⁵, D. Haidt¹⁰, L. Hajduk⁶, J. Haller¹³, B. Heinemann¹⁸,
 G. Heinzelmann¹¹, R.C.W. Henderson¹⁷, H. Henschel³⁵, O. Henshaw³, R. Heremans⁴,
 G. Herrera^{7,44}, I. Herynek²⁹, M. Hildebrandt³⁷, M. Hilgers³⁶, K.H. Hiller³⁵, J. Hladký²⁹,
 P. Höting², D. Hoffmann²², R. Horisberger³², A. Hovhannisyan³⁴, M. Ibbotson²¹,
 M. Jacquet²⁶, L. Janauschek²⁵, X. Janssen⁴, V. Jemanov¹¹, L. Jönsson²⁰, C. Johnson³,
 D.P. Johnson⁴, M.A.S. Jones¹⁸, H. Jung^{20,10}, D. Kant¹⁹, M. Kapichine⁸, M. Karlsson²⁰,
 J. Katzy¹⁰, F. Keil¹⁴, N. Keller³⁷, J. Kennedy¹⁸, I.R. Kenyon³, C. Kiesling²⁵, M. Klein³⁵,
 C. Kleinwort¹⁰, T. Kluge¹, G. Knies¹⁰, B. Koblitz²⁵, S.D. Kolya²¹, V. Korbel¹⁰, P. Kostka³⁵,
 R. Koutouev¹², A. Koutov⁸, A. Kropivnitskaya²³, J. Kroseberg³⁷, J. Kueckens¹⁰, T. Kuhr¹⁰,
 M.P.J. Landon¹⁹, W. Lange³⁵, T. Laštovička^{35,30}, P. Laycock¹⁸, A. Lebedev²⁴, B. Leißner¹,
 R. Lemrani¹⁰, V. Lendermann¹⁴, S. Levonian¹⁰, B. List³⁶, E. Lobodzinska^{10,6},
 N. Loktionova²⁴, R. Lopez-Fernandez¹⁰, V. Lubimov²³, H. Lueders¹¹, S. Lüders³⁷,
 D. Lüke^{7,10}, L. Lytkin¹², A. Makankine⁸, N. Malden²¹, E. Malinovski²⁴, S. Mangano³⁶,
 P. Marage⁴, J. Marks¹³, R. Marshall²¹, H.-U. Martyn¹, J. Martyniak⁶, S.J. Maxfield¹⁸,
 D. Meer³⁶, A. Mehta¹⁸, K. Meier¹⁴, A.B. Meyer¹¹, H. Meyer³³, J. Meyer¹⁰, S. Michine²⁴,
 S. Mikocki⁶, I. Milcewicz-Mika⁶, D. Milstead¹⁸, F. Moreau²⁷, A. Morozov⁸, J.V. Morris⁵,
 K. Müller³⁷, P. Murín^{16,42}, V. Nagovizin²³, B. Naroska¹¹, J. Naumann⁷, Th. Naumann³⁵,
 P.R. Newman³, F. Niebergall¹¹, C. Niebuhr¹⁰, D. Nikitin⁸, G. Nowak⁶, M. Nozicka³⁰,
 B. Olivier¹⁰, J.E. Olsson¹⁰, D. Ozerov²³, V. Panassik⁸, C. Pascaud²⁶, G.D. Patel¹⁸, M. Peez²²,
 E. Perez⁹, A. Petrukhin³⁵, J.P. Phillips¹⁸, D. Pitzl¹⁰, R. Pöschl²⁶, B. Povh¹², N. Raicevic³⁵,
 J. Rauschenberger¹¹, P. Reimer²⁹, B. Reisert²⁵, C. Risler²⁵, E. Rizvi³, P. Robmann³⁷,
 R. Roosen⁴, A. Rostovtsev²³, S. Rusakov²⁴, K. Rybicki^{6†}, D.P.C. Sankey⁵, E. Sauvan²²,
 S. Schätzel¹³, J. Scheins¹⁰, F.-P. Schilling¹⁰, P. Schleper¹⁰, D. Schmidt³³, S. Schmidt²⁵,
 S. Schmitt³⁷, M. Schneider²², L. Schoeffel⁹, A. Schöning³⁶, V. Schröder¹⁰,
 H.-C. Schultz-Coulon¹⁴, C. Schwanenberger¹⁰, K. Sedlák²⁹, F. Sefkow¹⁰, I. Sheviakov²⁴,
 L.N. Shtarkov²⁴, Y. Sirois²⁷, T. Sloan¹⁷, P. Smirnov²⁴, Y. Soloviev²⁴, D. South²¹, V. Spaskov⁸,
 A. Specka²⁷, H. Spitzer¹¹, R. Stamen¹⁰, B. Stella³¹, J. Stiewe¹⁴, I. Strauch¹⁰, U. Straumann³⁷,
 G. Thompson¹⁹, P.D. Thompson³, F. Tomasz¹⁴, D. Traynor¹⁹, P. Truöl³⁷, G. Tsipolitis^{10,38},
 I. Tsurin³⁵, J. Turnau⁶, J.E. Turney¹⁹, E. Tzamariudaki²⁵, A. Uraev²³, M. Urban³⁷, A. Usik²⁴,

S. Valkár³⁰, A. Valkárová³⁰, C. Vallée²², P. Van Mechelen⁴, A. Vargas Trevino⁷, S. Vassiliev⁸, Y. Vazdik²⁴, C. Veelken¹⁸, A. Vest¹, A. Vichnevski⁸, V. Volchinski³⁴, K. Wacker⁷, J. Wagner¹⁰, B. Waugh²¹, G. Weber¹¹, R. Weber³⁶, D. Wegener⁷, C. Werner¹³, N. Werner³⁷, M. Wessels¹, B. Wessling¹¹, M. Winde³⁵, G.-G. Winter¹⁰, Ch. Wissing⁷, E.-E. Woehrling³, E. Wünsch¹⁰, J. Žáček³⁰, J. Zálešák³⁰, Z. Zhang²⁶, A. Zhokin²³, F. Zomer²⁶, and M. zur Nedden²⁵

¹ *I. Physikalisches Institut der RWTH, Aachen, Germany^a*

² *III. Physikalisches Institut der RWTH, Aachen, Germany^a*

³ *School of Physics and Astronomy, University of Birmingham, Birmingham, UK^b*

⁴ *Inter-University Institute for High Energies ULB-VUB, Brussels; Universiteit Antwerpen, Antwerpen; Belgium^c*

⁵ *Rutherford Appleton Laboratory, Chilton, Didcot, UK^b*

⁶ *Institute for Nuclear Physics, Cracow, Poland^d*

⁷ *Institut für Physik, Universität Dortmund, Dortmund, Germany^a*

⁸ *Joint Institute for Nuclear Research, Dubna, Russia*

⁹ *CEA, DSM/DAPNIA, CE-Saclay, Gif-sur-Yvette, France*

¹⁰ *DESY, Hamburg, Germany*

¹¹ *Institut für Experimentalphysik, Universität Hamburg, Hamburg, Germany^a*

¹² *Max-Planck-Institut für Kernphysik, Heidelberg, Germany*

¹³ *Physikalisches Institut, Universität Heidelberg, Heidelberg, Germany^a*

¹⁴ *Kirchhoff-Institut für Physik, Universität Heidelberg, Heidelberg, Germany^a*

¹⁵ *Institut für experimentelle und Angewandte Physik, Universität Kiel, Kiel, Germany*

¹⁶ *Institute of Experimental Physics, Slovak Academy of Sciences, Košice, Slovak Republic^{e,f}*

¹⁷ *Department of Physics, University of Lancaster, Lancaster, UK^b*

¹⁸ *Department of Physics, University of Liverpool, Liverpool, UK^b*

¹⁹ *Queen Mary and Westfield College, London, UK^b*

²⁰ *Physics Department, University of Lund, Lund, Sweden^g*

²¹ *Physics Department, University of Manchester, Manchester, UK^b*

²² *CPPM, CNRS/IN2P3 - Univ Mediterranee, Marseille - France*

²³ *Institute for Theoretical and Experimental Physics, Moscow, Russia^l*

²⁴ *Lebedev Physical Institute, Moscow, Russia^e*

²⁵ *Max-Planck-Institut für Physik, München, Germany*

²⁶ *LAL, Université de Paris-Sud, IN2P3-CNRS, Orsay, France*

²⁷ *LLR, Ecole Polytechnique, IN2P3-CNRS, Palaiseau, France*

²⁸ *LPNHE, Universités Paris VI and VII, IN2P3-CNRS, Paris, France*

²⁹ *Institute of Physics, Academy of Sciences of the Czech Republic, Praha, Czech Republic^{e,i}*

³⁰ *Faculty of Mathematics and Physics, Charles University, Praha, Czech Republic^{e,i}*

³¹ *Dipartimento di Fisica Università di Roma Tre and INFN Roma 3, Roma, Italy*

³² *Paul Scherrer Institut, Villigen, Switzerland*

³³ *Fachbereich Physik, Bergische Universität Gesamthochschule Wuppertal, Wuppertal, Germany*

³⁴ *Yerevan Physics Institute, Yerevan, Armenia*

³⁵ *DESY, Zeuthen, Germany*

³⁶ *Institut für Teilchenphysik, ETH, Zürich, Switzerland^j*

³⁷ *Physik-Institut der Universität Zürich, Zürich, Switzerland^j*

³⁸ Also at Physics Department, National Technical University, Zografou Campus, GR-15773 Athens, Greece

³⁹ Also at Rechenzentrum, Bergische Universität Gesamthochschule Wuppertal, Germany

⁴⁰ Also at Institut für Experimentelle Kernphysik, Universität Karlsruhe, Karlsruhe, Germany

⁴¹ Also at Dept. Fis. Ap. CINVESTAV, Mérida, Yucatán, México^k

⁴² Also at University of P.J. Šafárik, Košice, Slovak Republic

⁴³ Also at CERN, Geneva, Switzerland

⁴⁴ Also at Dept. Fis. CINVESTAV, México City, México^k

[†] Deceased

^a Supported by the Bundesministerium für Bildung und Forschung, FRG, under contract numbers 05 H1 1GUA /1, 05 H1 1PAA /1, 05 H1 1PAB /9, 05 H1 1PEA /6, 05 H1 1VHA /7 and 05 H1 1VHB /5

^b Supported by the UK Particle Physics and Astronomy Research Council, and formerly by the UK Science and Engineering Research Council

^c Supported by FNRS-FWO-Vlaanderen, IISN-IIKW and IWT and by Inter-University Attraction Poles Programme, Belgian Science Policy

^d Partially Supported by the Polish State Committee for Scientific Research, SPUB/DESY/P003/DZ-118/2003/2005

^e Supported by the Deutsche Forschungsgemeinschaft

^f Supported by VEGA SR grant no. 2/1169/2001

^g Supported by the Swedish Natural Science Research Council

ⁱ Supported by the Ministry of Education of the Czech Republic under the projects INGO-LA116/2000 and LN00A006, by GAUK grant no 173/2000

^j Supported by the Swiss National Science Foundation

^k Supported by CONACyT

^l Partially Supported by Russian Foundation for Basic Research, grant no. 00-15-96584

Dedicated to the memory of Krzysztof Rybicki.

1 Introduction

Measurements of the hadronic final state in deep-inelastic positron-proton scattering (DIS) at HERA have allowed precision tests of the theory of the strong force, Quantum Chromodynamics (QCD). In particular, properties of the hadronic final state in the region near to the proton remnant system (hereafter referred to as the ‘forward region’) have been shown to be sensitive to the QCD radiation pattern formed from the cascade initiated by a parton from the proton before it undergoes a hard scatter [1–4]. This paper presents studies made by the H1 experiment of DIS interactions at values of Bjorken- x down to $x \approx 4 \cdot 10^{-5}$ containing at least one high transverse momentum, forward going π^0 -meson.

A generic diagram for parton evolution in a DIS process at low x in which a gluon from the proton undergoes a QCD cascade is shown in Fig. 1 (a). The gluon eventually interacts with the virtual photon via a hard photon-gluon fusion process which can be calculated within perturbative QCD using an exact matrix element. Several perturbative QCD-based prescriptions are available to describe the dynamics of the parton evolution process. The Dokshitzer-Gribov-Lipatov-Altarelli-Parisi (DGLAP) evolution equations [5] resum leading $\log(Q^2)$ terms and ignore $\log(1/x)$ terms. In an axial gauge this corresponds to the resummation of diagrams in which the parton cascades follow a strong ordering in transverse momenta $k_{Tn}^2 \gg k_{Tn-1}^2 \gg \dots \gg k_{T1}^2$. At sufficiently small values of x the Balitsky-Fadin-Kuraev-Lipatov (BFKL) equation [6] should be applicable since the $\log(1/x)$ terms should dominate the evolution. In this scheme the cascade is ordered strongly in fractional momenta $x_n \ll x_{n-1} \ll \dots \ll x_1$, while the transverse momenta perform a ‘random walk’ with k_{Ti} being close to k_{Ti-1} , though it can be both larger or smaller. The Ciafaloni-Catani-Fiorani-Marchesini (CCFM) equation [7] interpolates between the DGLAP and BFKL approximations with parton emissions ordered in angle.

A parton chain without a requirement of k_T ordering throughout the complete cascade is provided in a picture of low x DIS in which the virtual photon is ascribed a partonic structure. This process is illustrated in Fig. 1 (b) in which k_T -ordered DGLAP cascades are initiated both from the proton and photon, leading to the hard interaction at the centre of the QCD ‘ladder’.

Hadronic final state observables are sensitive to the dynamics of QCD processes and are thus expected to be able to discriminate between different evolution approximations. As illustrated in Fig. 1, the selection of leading particles or jets in the forward region can tag individual parton emissions at high transverse momentum. An advantage of using single particles rather than jets is that ambiguities due to the choice of jet algorithm are removed. On the other hand, uncertainties due to hadronisation are typically larger for single particle studies. As was pointed out in [8], the selection of particles or jets with values of transverse momentum squared of similar magnitude to Q^2 suppresses the contribution of k_T -ordered cascades with respect to k_T -unordered processes. In addition, the phase space for BFKL effects is enhanced if the fraction of the proton’s energy of the particle or jet is required to be greater than Bjorken- x .

A recent H1 study of forward going π^0 -mesons [9] found that a model which implemented a DGLAP parton cascade from the proton significantly underestimated the cross section at low values of Bjorken- x . Leading order BFKL calculations with kinematic constraints which mimic higher orders and a model implementing virtual photon structure gave a better description of the data.

The pseudorapidity dependence of the mean transverse energy produced in an event (the so-called transverse energy flow) provides a complementary means of studying the hadronic final state. Compared with studies of jets and high transverse momentum particles, measurements of transverse energy flow typically cover a wider range of pseudorapidity and are sensitive to parton emissions of lower transverse momentum. Previous measurements of transverse energy flow at HERA were indeed found to be sensitive to the modelling of both the perturbative QCD evolution and the soft hadronisation process [1, 10, 11]. Measurements of transverse energy flow in events containing particles with high transverse momentum also reveal the range over which transverse momentum is compensated following the emission of QCD radiation [12].

This paper presents a study of low x DIS interactions in which high transverse momentum π° -mesons are produced in the forward region. The results are based on a data sample which is more than three times larger than that used for earlier studies [9]. Consequently, the inclusive π° cross section is measured with greater precision and more differentially as a function of x , Q^2 and the transverse momentum and energy of the π° -meson. Furthermore, for the first time, measurements are presented of transverse energy flow for ep interactions containing forward going π° -mesons. This allows a more complete investigation of hadronic final states containing a hard forward π° than was previously possible.

2 QCD-based Models

Calculations of the expected production rate of π° -mesons and the associated transverse energy flow in DIS are available in the form of Monte Carlo event generators. These use first-order QCD matrix elements and adopt various approaches to modelling the parton cascade. These models are used to provide comparisons of theory predictions with the measurements presented here. In addition they are used, together with a simulation of the H1 detector, to correct the measurements for the finite acceptance and resolution of the detector. Unless otherwise stated the proton and virtual photon parton densities used in these models are CTEQ6M [13] and SAS-1D [14], respectively.

LEPTO 6.51 [15] matches first-order QCD matrix elements to DGLAP-based leading-log parton showers. The factorisation and renormalisation scales are set to Q^2 . LEPTO also allows for non-perturbative rearrangement of the event colour topology via so-called soft color interactions in the final state [16].

RAPGAP 2.08/20 [17] also matches first-order QCD matrix elements for direct photon processes to DGLAP-based leading-log parton showers. In addition to the direct photon processes, RAPGAP simulates resolved photon interactions in which the virtual photon is assumed to have partonic structure. For the predictions presented here, the renormalisation and factorisation scales are set to $4p_T^2 + Q^2$, where p_T is the transverse momentum of the partons emerging from the hard scattering process. The hadronic final state predictions of RAPGAP, when only direct photon interactions are considered, are very similar to those of LEPTO.

ARIADNE 4.10 [18] is an implementation of the Colour Dipole Model (CDM) [19] of a chain of independently radiating dipoles formed by emitted gluons. Since all radiation is assumed to come from the dipole formed by the struck quark and the remnant, photon-gluon fusion events

have to be added and are taken from the QCD matrix elements. The parameters in ARIADNE have been optimised in order to describe a range of hadronic final state measurements [20].

In order to study the effects of initial and final state QED radiation, the above models are interfaced with HERACLES [21] within the DJANGO [22] model.

CASCADE 1.0 [23] uses off-shell QCD matrix elements, supplemented with parton emissions based on the CCFM equation within a backward evolution approach. An unintegrated gluon density, obtained using CCFM evolution and fitted to describe the inclusive DIS cross section [24], is used as an input to this model. In the present analysis an updated version [25] of CASCADE with an improved treatment of the soft region and a new parameterisation of the unintegrated gluon density is used. These modifications provide an improved description of forward jet production [26].

To perform the hadronisation step, all of the above models use the LUND string fragmentation [27] scheme, as implemented in JETSET [28] in case of LEPTO, RAPGAP and ARIADNE and in PYTHIA [28] for CASCADE.

Predictions of the π° cross sections are also available from an analytical calculation at the parton level [29] based on a modified BFKL evolution equation at lowest order. These calculations are then convoluted with a π° fragmentation function [30]. The proton parton densities are taken from [31]. The modified evolution equation imposes a ‘‘consistency constraint’’ [32, 33] which, it is argued, mimics much of the contribution from non-leading $\log(1/x)$ terms to the BFKL equation. However, these predictions are very sensitive to the choice of scale for the strong coupling constant α_s and to the infra-red cut-off. In the present analysis, the scale for α_s is taken to be the squared transverse momentum of the emitted partons, k_T^2 , and the infrared cut-off in the modified BFKL equation is set at 0.5 GeV^2 .

Recently, calculations of the cross section for the production of high transverse momentum hadrons in DIS interactions have been made [34], which describe earlier measurements of forward π° production [9]. These comprise next-to-leading order (NLO) matrix elements, convoluted with NLO fragmentation functions [30]. The proton parton densities MRST99 (higher gluon) [35] are used. For comparison with the H1 data, the renormalisation, factorisation and fragmentation scales are each set to $(Q^2 + p_{T,\pi}^{*2})/2$, where $p_{T,\pi}^*$ is the transverse momentum, in the photon-proton centre of mass system¹, of the parton which fragments into the forward π° . In these calculations, a large part of the cross section is generated by higher order contributions which correspond to lowest order BFKL and resolved photon processes [34].

3 Experimental Apparatus

A detailed description of the H1 detector can be found elsewhere [36]. The following section briefly describes the components of the detector which are most relevant for this analysis.

A liquid argon (LAr) calorimeter is used to measure the hadronic energy flow and the candidate π° -meson properties. The LAr calorimeter provides measurements over the laboratory

¹All quantities presented in the hadronic centre-of-mass system are denoted by the superscript *.

polar angle range $4^\circ < \theta < 154^\circ$, where θ is defined with respect to the direction of the proton beam, and offers full azimuthal coverage. It consists of an electromagnetic section with lead absorbers and a hadronic section with steel absorbers. Both sections are highly segmented in the transverse and longitudinal directions. The total depth of both sections varies between 4.5 and 8 interaction lengths in the region $4^\circ < \theta < 128^\circ$, and between 20 and 30 radiation lengths in the region $4^\circ < \theta < 154^\circ$ increasing towards the forward direction. The fine granularity of the electromagnetic section in the forward direction is characterized by four-fold longitudinal segmentation and a typical lateral cell size of $3.5 \times 3.5 \text{ cm}^2$. Test beam measurements of the LAr calorimeter modules showed an energy resolution of $\sigma_E/E \approx 0.50/\sqrt{E[\text{GeV}]} \oplus 0.02$ for charged pions and of $\sigma_E/E \approx 0.12/\sqrt{E[\text{GeV}]} \oplus 0.01$ for electrons [36]. The hadronic energy measurement is made by applying a weighting technique to the electromagnetic and hadronic components of the energy deposition, in order to account for the non-compensating nature of the calorimeter. The absolute scales of hadronic and forward-reconstructed electromagnetic energies are known to 4% [37] and 3% [38], respectively.

The SPACAL is a lead/scintillating fibre calorimeter covering the region $153^\circ < \theta < 177.5^\circ$ with an electromagnetic and a hadronic section. It is used to measure the scattered positron energy and the backward hadronic energy flow. The energy resolutions for electrons and hadrons are $\sigma_E/E \approx 0.07/\sqrt{E[\text{GeV}]} \oplus 0.01$ [39] and $\sigma_E/E \approx 0.3/\sqrt{E[\text{GeV}]} \oplus 0.01$ [40], respectively. The energy scale uncertainties are 1% for electrons and 7% for hadrons [41].

The calorimeters are surrounded by a superconducting solenoid which provides a uniform magnetic field of 1.15 T in a direction parallel to the proton beam in the tracking region. Charged particle tracks are measured in the central tracker (CT) and forward tracker (FT) systems which cover the polar angle ranges of $25^\circ < \theta < 155^\circ$ and $5^\circ < \theta < 25^\circ$, respectively. Information from the CT is used in this work to trigger events, to locate the event vertex and also contributes to the measurement of transverse energy.

A backward drift chamber (BDC) in front of the SPACAL with an angular acceptance of $151^\circ < \theta < 177.5^\circ$ serves to identify electron candidates and to precisely measure their direction. Using information from the BDC, the SPACAL and the reconstructed event vertex position, the polar angle of the scattered electron is known to about 0.5 mrad [41].

The luminosity is measured using the Bethe-Heitler process $ep \rightarrow ep\gamma$ with two TICI/TIBr crystal calorimeters installed in the HERA tunnel.

4 Data Analysis

The data used for this analysis were collected in 1996 and 1997 when positrons and protons with energies of 27.6 GeV and 820 GeV, respectively, were collided. The data-set used in this work corresponds to an integrated luminosity of 21.2 pb^{-1} .

4.1 DIS Event Selection

DIS events are selected by triggers based on electromagnetic energy deposits in the SPACAL calorimeter and the presence of charged particle tracks in the CT. For the π^0 -enriched event

sample, the trigger efficiency lies between 60% and 80%, determined using independently triggered data. The inefficiency is mainly due to the suppression by the trigger of events with less than 3 charged particles measured in the CT. The data are corrected for the trigger inefficiency by applying a weight to every selected DIS event.

The event kinematics are calculated from the polar angle and the energy of the scattered positron. In order to maintain optimal efficiency and acceptance, scattered positron candidates in the SPACAL are required to have an energy $E_{e'} > 10$ GeV and to lie in the region of polar angle of $156^\circ < \theta_{e'} < 177^\circ$. The data-set is further restricted to the kinematic range in inelasticity y and virtuality Q^2 of $0.1 < y < 0.6$ and $2 < Q^2 < 70$ GeV², respectively. The resulting values of Bjorken- x extend over two orders of magnitude in the range $4 \cdot 10^{-5} < x < 6 \cdot 10^{-3}$.

To further reject background from photoproduction interactions in which a particle from the hadronic final state is misidentified as a scattered positron in the SPACAL, the condition $35 < \sum_j (E_j - p_{z,j}) < 70$ GeV is applied. Here E_j and $p_{z,j}$ are the energy and longitudinal momentum, respectively, of a particle, and the sum extends over all particles in the event except those detected in the luminosity system.

4.2 Forward π° Selection

The selection of forward π° -mesons closely follows that of earlier work [3, 9, 42]. The π° candidates are identified via the dominant decay channel $\pi^\circ \rightarrow 2\gamma$ using calorimetric information only. Criteria are placed on the kinematic properties of the candidate to ensure high acceptance and efficient background rejection. The energy E_π of the π° scaled with the energy E_p of the proton beam, $x_\pi = E_\pi/E_p$, is required to be greater than 0.01. As a consequence of this cut, the decay photons are not resolved individually but are merged into a single electromagnetic cluster in the detector. The candidates are also required to lie in the polar angle region $5^\circ < \theta_\pi < 25^\circ$. This polar angle region, referred to as ‘forward’ in the laboratory frame, corresponds to the central region in the hadronic centre of mass frame, $-1.25 \lesssim \eta_\pi^* \lesssim 2.0$. Furthermore, the π° transverse momentum in the photon-proton centre of mass system, $p_{T,\pi}^*$ must be greater than 2.5 GeV. The Lorentz boost to this frame is calculated using the kinematics of the scattered electron. In this frame the proton direction is chosen to define the negative z^* axis.

Electromagnetic and hadronic showers are discriminated by an analysis of the longitudinal and transverse shapes of the energy depositions. A π° candidate is required to have more than 90% of its energy deposited in the electromagnetic part of the LAr calorimeter. A ‘‘hot’’ core of the most energetic group of contiguous cells within a cluster, which must include the hottest cell, is required to account for over 50% of the cluster energy. The lateral spread of the shower, defined as in [43], is required to be less than 4 cm. Electromagnetic clusters with a small longitudinal extent are selected by requiring that the difference in the amounts of energy found in the second and fourth longitudinal layers of the electromagnetic calorimeter must be more than 40% of the total cluster energy.

Following this selection approximately 5500 (2000) π° candidates remain after the transverse momentum cut $p_{T,\pi}^* > 2.5$ (3.5) GeV. Using simulated events generated with the LEPTO

and ARIADNE models the efficiency of the selection is estimated to be approximately 45%, and the contribution of non- π^0 background is about 20%.

The contamination of the sample from sources of high energy single photons other than π^0 decays, such as prompt photon production, is expected to be negligible since the rate of such processes is low [44]. Using the LEPTO and ARIADNE models the total contamination due to the misidentification of electrons, and of η -mesons decaying to two photons, is found to be less than 4%. The measurements are corrected for this using the QCD-based models following the procedure outlined in section 4.3. The contribution of the background from photoproduction processes was studied using the PHOJET [45] model and found to be negligible.

4.3 Correction Procedure and Systematic Uncertainties

The results shown in this paper consist of two sets of spectra. First, the dependence of the ep cross section for inclusive forward π^0 -meson production on Bjorken- x , Q^2 , $p_{T,\pi}^*$ and x_π is studied. Measurements are then presented of the transverse energy flow in π^0 -tagged events. The transverse energy is evaluated from energy deposits measured in the LAr and SPACAL calorimeters, supplemented with tracking information from the CT, according to the prescription in [46].

The data are corrected using a bin-by-bin unfolding procedure using event samples generated with the LEPTO and ARIADNE models. The correction factors are obtained by taking the average of the correction factors estimated by these two models. The typical values of the correction factors obtained are approximately equal to 1.5.

The following sources of systematic uncertainty are considered. The uncertainties from each source are added quadratically to form the total point-to-point systematic uncertainties on each of the measured distributions presented here:

- The model dependence of the bin-by-bin acceptance corrections leads to systematic uncertainties of between 4% and 11% on both the π^0 cross section and transverse energy spectra. This source of uncertainty is calculated as half the difference of the correction factors derived from LEPTO and ARIADNE. The uncertainty resulting from the model dependence is largest at the lowest values of x and for the highest values of $p_{T,\pi}^*$ and x_π .
- The systematic uncertainty due to the correction for QED radiative effects, calculated using HERACLES, is typically 3% for both the π^0 cross section and the transverse energy flow measurements.
- Variation of the π^0 selection and identification cuts within the resolution of the reconstructed quantities gives rise to an uncertainty of 5% to 10% in the measurements of both the cross section and the transverse energy flow.
- The uncertainty on the electromagnetic energy scale of the SPACAL (1%) affects the reconstructed kinematics of the scattered positron. This results in uncertainties on the π^0 cross section and the transverse energy flow measurements of typically 9% and 2%, respectively.

- The uncertainty on the electromagnetic energy scale of the LAr (3%) leads to an uncertainty on the π° cross section of 5% to 10%, but has a negligible impact on the transverse energy spectra.
- The hadronic energy scale uncertainty on the LAr (4%) gives rise to an uncertainty on the transverse energy flow measurements of 4%, but has negligible impact on the π° cross sections.
- The uncertainty on the hadronic energy scale of the SPACAL (7%) results in uncertainties on the π° cross section and the transverse energy flow measurements of typically 2% and 5%, respectively.
- The uncertainty on the polar angle measurement of the scattered electron (0.5 mrad) has a small influence (below 2%) on the π° cross section and the transverse energy flow spectra.
- The uncertainty on the determination of the trigger efficiency leads to a 5% uncertainty on the π° cross section measurements, but has a negligible effect on the transverse energy flow spectra.
- The uncertainty on the luminosity measurement leads to a 1.5% uncertainty on the π° cross section measurement, but has no effect on the transverse energy distributions.

5 Results

5.1 Inclusive Forward π° Cross Sections

The inclusive π° cross section is measured differentially as a function of Q^2 and x , and as a function of $p_{T,\pi}^*$ and x_π , for π° -mesons produced in the range $p_{T,\pi}^* > 2.5$ GeV, $5^\circ < \theta_\pi < 25^\circ$ and $x_\pi > 0.01$. The DIS phase space is restricted to the kinematic range $2 < Q^2 < 70$ GeV² and $0.1 < y < 0.6$. The cross section data presented in this section are also given in Tables 1 and 2.

The inclusive cross section $d\sigma_\pi/dx$ for $p_{T,\pi}^* > 2.5$ GeV as a function of Bjorken x is shown in Fig. 2 for three intervals of Q^2 : $2 < Q^2 \leq 4.5$ GeV²; $4.5 < Q^2 \leq 15$ GeV² and $15 < Q^2 < 70$ GeV². The distributions rise with falling x except at values of x of around 10^{-4} in the lowest Q^2 region. This turnover is due to the limitations in the phase space imposed by the π° and DIS event selection cuts.

The predictions of five QCD-based models are compared with the data. Calculations from RAPGAP which implement DGLAP evolution for proton structure only, labelled DIR, fall substantially below the data. The disagreement becomes more pronounced at lower values of Bjorken- x . Calculations which assume virtual photon structure, marked DIR+RES, describe the data well, although it is necessary to use rather large renormalisation and factorisation scales, $\mu^2 = Q^2 + 4p_T^2$, in order to get a sufficiently large resolved photon component. Using the same scale in RAPGAP a reasonable description of the azimuthal jet separation in a measurement of inclusive dijet production at low x in DIS [47] is obtained. Forward jet data are also well

described by DGLAP-based calculations which include virtual photon structure although different measurements tend to prefer different choices of scales [3, 4, 26], $\mu^2 = Q^2 + 4p_T^2$ or $\mu^2 = Q^2 + p_T^2$. Using the latter value would result in a reduction of about 30% in the normalisation of the predicted forward π° distributions measured in this paper, with little change to the shape. Predictions based on the CCFM equation, labelled CCFM (CASCADE), agree at the highest values of Q^2 . However, they fall below the data at low values of x and Q^2 . The rate of forward jet events predicted by CASCADE agrees with the data [26]. This observation is not in contradiction with the forward π° data since the discrepancies observed here arise at the lowest values of x , which are not covered by the forward jet measurement. Differences between RAPGAP and CASCADE in the overall description of forward jet and particle production may be related to differences in the modelling of the partonic structure of forward jets. CASCADE mostly produces gluon-induced jets, while RAPGAP has a substantial contribution of quark-induced jets in the forward region. Fewer high momentum particles are produced in gluon-induced jets than in quark-induced jets [48]. Predictions of the CDM give a reasonable description of the data. Analytical calculations using a modified BFKL equation, labelled mod. LO BFKL, describe the data well in the lower Q^2 region although they have a tendency to exceed the data at the lowest values of Bjorken- x in the highest Q^2 intervals.

Fig. 3 shows the differential cross section $d\sigma_\pi/dx$ for transverse momenta $p_{T,\pi}^* > 3.5$ GeV, in three intervals of Q^2 : $2 < Q^2 \leq 8$ GeV²; $8 < Q^2 \leq 20$ GeV² and $20 < Q^2 < 70$ GeV². Compared with the spectra in Fig. 2, the measured differential cross sections are lower by factors of between two and four. The QCD-based models provide a similar quality of description to that given in Fig. 2. Calculations based on the modified BFKL equation clearly exceed the data in the two highest Q^2 intervals. The prediction of the NLO calculation [34] is also shown and describes the data well. Predictions of the CDM (not shown) overestimate the data at the lowest values of Q^2 and x .

The cross section $d\sigma_\pi/dp_{T,\pi}^*$ is shown as a function of $p_{T,\pi}^*$ in Fig. 4 in the same Q^2 intervals as in Fig. 2. The data fall steeply with increasing $p_{T,\pi}^*$ and the shapes of the distributions vary only slightly with increasing Q^2 . The calculations implementing resolved virtual photons describe the data well. The predictions of the model including only direct processes fall below the data everywhere although they come nearer to the data as Q^2 increases. The CCFM-based calculations fail in the lowest Q^2 interval but give a reasonable description of the highest Q^2 interval. The CDM predicts spectra which are somewhat harder than the data.

In Fig. 5 the cross section $d\sigma_\pi/dx_\pi$ is shown as a function of x_π in the same three intervals of Q^2 as used in Fig. 2. In Fig. 6 the differential cross section is presented in three intervals of Bjorken- x : $4.2 \cdot 10^{-5} < x \leq 2 \cdot 10^{-4}$; $2 \cdot 10^{-4} < x \leq 10^{-3}$ and $10^{-3} < x < 6.3 \cdot 10^{-3}$. The cross section falls as x_π increases. There is no strong dependence of the shapes of the distributions on Bjorken- x or Q^2 . The resolved photon approach, the CDM, and the BFKL calculations describe the spectra well. The CCFM implementation describes the data only in the highest intervals of Q^2 and x . The direct photon calculations fall below the data in all of the spectra but approach them as Q^2 increases.

5.2 Transverse Energy Flow

The transverse energy flow, defined as the mean transverse energy per event per unit of pseudorapidity difference in the hadronic centre of mass system, $\frac{1}{N}dE_T^*/d(\eta^* - \eta_\pi^*)$, in events containing at least one forward π° is presented in Fig. 7. Here N is the total number of events and E_T^* is the sum of the transverse energies of each particle i : $E_T^* = \sum_i E_{Ti}^*$. The transverse energy E_{Ti}^* of a particle i with energy E_i^* and polar angle θ_i^* is defined as $E_{Ti}^* = E_i^* \sin \theta_i^*$. The pseudorapidity η^* is defined as $-\ln \tan(\theta^*/2)$. The energy flow, which includes the contribution from the forward π° , is plotted as a function of the difference in pseudorapidity $\eta^* - \eta_\pi^*$ from the selected forward π° . In events containing more than one forward π° , the candidate with the largest transverse momentum is chosen. The spectra are presented in three intervals of the π° pseudorapidity ranging from close (Fig. 7a) to far (Fig. 7c) from the proton direction.

The spectra show a large increase of transverse energy production in the region associated with the π° . This can be understood as being due to the energy associated with the jet which contains the leading π° . A broad distribution of lower transverse energy flow in the current region reveals the range over which the transverse momentum of the jet is compensated.

The QCD-based models all describe the transverse energy flow in the vicinity of the π° but give different predictions in the current region. Calculations with resolved photon processes tend to agree best with the data. The CCFM approach provides a reasonable description of the data. This model predicts a strong compensation of the π° transverse momentum in the rapidity region between the forward particle and the proton remnant system which is, however, not covered in the measurements presented here. The direct photon model shows a peak at larger values of pseudorapidity difference $\eta^* - \eta_\pi^*$ than is observed in the data. This effect becomes less pronounced with increasing π° pseudorapidity as the forward π° may enter the current jet region. The differences between the models can be qualitatively understood as a consequence of the ordering or otherwise of the k_T in the parton cascades. The k_T ordering in the direct photon model forces the compensation of the transverse energy in the current region while models without this requirement allow compensation close to the π° -meson. The CDM (not shown) predicts too much transverse energy in the vicinity of the π° . This is a consequence of the overly hard π° transverse momentum distribution predicted by the CDM and shown earlier in Fig. 4.

Transverse energy flow in the region away from the forward π° and into the current region is further studied as shown in Fig. 8. The mean transverse energy over the region $1.0 < \eta^* - \eta_\pi^* < 3.0$ is plotted as a function of Bjorken- x for the same three intervals of the π° pseudorapidity as in the previous figure. The data show no significant dependence on Bjorken- x although there is a tendency for the mean transverse energy to fall as pseudorapidity of π° approaches the current region. With the exception of the direct photon model, all of the QCD-based models give a reasonable description of the data. The direct photon prescription is only able to describe the data in the pseudorapidity region closest to the proton remnant.

6 Summary

Measurements are presented of ep interactions containing high transverse momentum forward going π° -mesons in the deep-inelastic scattering regime of $0.1 < y < 0.6$, $2 < Q^2 < 70 \text{ GeV}^2$

and $4 \cdot 10^{-5} < x < 6 \cdot 10^{-3}$. The inclusive π^0 cross section is measured differentially as a function of Q^2 , Bjorken- x and π^0 transverse momentum and energy for particles with $p_{T,\pi}^* > 2.5$ GeV, $5^\circ < \theta_\pi < 25^\circ$ and $x_\pi = \frac{E_\pi}{E_p} > 0.01$. The transverse energy flow relative to the direction of the forward π^0 and the mean transverse energy in the vicinity of the forward π^0 are also measured.

The measurements presented are sensitive to the dynamics of parton evolution. Several different QCD-based approaches are confronted with the data. An approach implementing DGLAP evolution of proton structure underestimates the π^0 cross section at low values of Bjorken- x and Q^2 and overestimates the range at which the π^0 transverse momentum is compensated. Calculations implementing virtual photon structure provide the best description, albeit with a preferred choice of renormalisation and factorisation scale which is inconsistent with that required by other measurements of the hadronic final state in the forward region. Predictions based on CCFM evolution fail to describe the π^0 cross section at the lowest values of Bjorken- x but give a fair description of the transverse energy distributions. The Colour Dipole Model gives a reasonable description of the π^0 cross section but predicts a transverse momentum distribution of π^0 -mesons which is significantly harder than is observed in the data. Calculations using next-to-leading order QCD matrix elements convoluted with π^0 fragmentation functions describe the Bjorken- x dependence of the forward π^0 cross section well. Predictions made using a modified BFKL equation describe the forward π^0 cross section at the lowest Q^2 values but exceed the data at the highest Q^2 values.

Acknowledgements

We would like to thank Alan Martin, John Outhwaite and the late Jan Kwieciński for making available the program to calculate forward jet and particle cross sections using the modified LO BFKL model. We are grateful to Patrik Aurenche, Michel Fontannaz, Rohini Godbole and Rahul Basu for providing their NLO calculations. We also thank Gunnar Ingelman for useful discussions. We are grateful to the HERA machine group whose outstanding efforts have made this experiment possible. We thank the engineers and technicians for their work in constructing and now maintaining the H1 detector, our funding agencies for financial support, the DESY technical staff for continual assistance and the DESY directorate for support and for the hospitality which they extend to the non-DESY members of the collaboration.

References

- [1] I. Abt *et al.* [H1 Collaboration], *Z. Phys.* **C 63** (1994) 377.
- [2] S. Aid *et al.* [H1 Collaboration], *Phys. Lett.* **B 356** (1995) 118 [hep-ex/9506012].
- [3] C. Adloff *et al.* [H1 Collaboration], *Nucl. Phys.* **B 538** (1999) 3 [hep-ex/9809028].
- [4] J. Breitweg *et al.* [ZEUS Collaboration], *Eur. Phys. J.* **C 6** (1999) 239 [hep-ex/9805016];
J. Breitweg *et al.* [ZEUS Collaboration], *Phys. Lett.* **B 474** (2000) 223 [hep-ex/9910043].

- [5] V. N. Gribov and L. N. Lipatov, Sov. J. Nucl. Phys. **15** (1972) 438 and 675;
 L. N. Lipatov, Sov. J. Nucl. Phys. **20** (1975) 94;
 G. Altarelli and G. Parisi, Nucl. Phys. **B 126** (1977) 298;
 Y. L. Dokshitzer, Sov. Phys. JETP **46** (1977) 641.
- [6] E. A. Kuraev, L. N. Lipatov and V. S. Fadin, Sov. Phys. JETP **45** (1977) 199;
 I. I. Balitsky and L. N. Lipatov, Sov. J. Nucl. Phys. **28** (1978) 822.
- [7] M. Ciafaloni, Nucl. Phys. **B 296** (1988) 49;
 S. Catani, F. Fiorani and G. Marchesini, Phys. Lett. **B 234** (1990) 339;
 S. Catani, F. Fiorani and G. Marchesini, Nucl. Phys. **B 336** (1990) 18;
 G. Marchesini, Nucl. Phys. **B 445** (1995) 49 [hep-ph/9412327].
- [8] A. H. Mueller, Nucl. Phys. Proc. Suppl. **18 C** (1991) 125;
 A. H. Mueller, J. Phys. **G 17** (1991) 1443.
- [9] C. Adloff *et al.* [H1 Collaboration], Phys. Lett. **B 462** (1999) 440 [hep-ex/9907030].
- [10] C. Adloff *et al.* [H1 Collaboration], Eur. Phys. J. **C 12** (2000) 595 [hep-ex/9907027].
- [11] M. Derrick *et al.* [ZEUS Collaboration], Phys. Lett. **B 356** (1995) 118 [hep-ex/9506012].
- [12] M. Arneodo *et al.* [European Muon Collaboration], Phys. Lett. **B 149** (1984) 415.
- [13] J. Pumplin *et al.*, JHEP **0207** (2002) 12 [hep-ph/0201195].
- [14] G. A. Schuler and T. Sjöstrand, Phys. Lett. **B 376** (1996) 193 [hep-ph/9601282].
- [15] G. Ingelman, A. Edin and J. Rathsman, Comp. Phys. Comm. **101** (1997) 108 [hep-ph/9605286].
- [16] G. Ingelman, A. Edin and J. Rathsman, Phys. Lett. **B 336** (1996) 371 [hep-ph/9508386].
- [17] H. Jung, Comp. Phys. Comm. **86** (1995) 147
 (for an update see <http://www-h1.desy.de/~jung/rapgap/rapgap.html>).
- [18] L. Lönnblad, Comp. Phys. Comm. **71** (1992) 15.
- [19] B. Andersson, G. Gustafson and L. Lönnblad, Nucl. Phys. **B 339** (1990) 393.
- [20] N. H. Brook *et al.* in *Monte Carlo Generators for HERA Physics* (Hamburg, Germany, 1999), A. T. Doyle, G. Grindhammer, G. Ingelman, H. Jung, Eds., DESY-PROC-1999-02, p.10 [hep-ex/9912053];
 G. Grindhammer, D. Krucker and G. Nellen, *ibid.* p.36.
- [21] A. Kwiatkowski, H. Spiesberger and H. J. Moring, Comp. Phys. Comm. **69** (1992) 155.
- [22] K. Charchula, G. A. Schuler and H. Spiesberger, Comp. Phys. Comm. **81** (1994) 381.
- [23] H. Jung, Comp. Phys. Comm. **143** (2002) 100 [hep-ph/0109102].
- [24] H. Jung and G. P. Salam, Eur. Phys. J. **C 19** (2001) 351 [hep-ph/0012143].

- [25] M. Hansson, H. Jung, “*The status of CCFM: Unintegrated gluon densities*”, to appear in Proc. of the XI Int. Workshop on Deep Inelastic Scattering (DIS 2003), St. Petersburg, Russia, April 2003 [hep-ph/0309009].
- [26] J. Andersen *et al.* [Small x Collaboration], “*Small x phenomenology: Summary and Status 2002*” [hep-ph/0312333].
- [27] B. Andersson, G. Gustafson, G. Ingelman and T. Sjöstrand, Phys. Rep. **97** (1983) 31.
- [28] T. Sjöstrand, Comp. Phys. Comm. **82** (1994) 74;
T. Sjöstrand *et al.* Comp. Phys. Comm. **135** (2001) 238 [hep-ph/0010017].
- [29] J. Kwieciński, A. D. Martin and J. J. Outhwaite, Eur. Phys. J. **C 9** (1999) 611 [hep-ph/9903439].
- [30] B. A. Kniehl, G. Kramer and B. Pötter, Nucl. Phys. **B 597** (2001) 337 [hep-ph/0011155].
- [31] A. D. Martin, R. G. Roberts, W. J. Stirling and R. S. Thorne, Eur. Phys. J. **C 4** (1998) 463 [hep-ph/9803445].
- [32] J. Kwieciński, A. D. Martin and P. J. Sutton, Z. Phys. **C 71** (1996) 585 [hep-ph/9602320].
- [33] J. Kwieciński, A. D. Martin and A. M. Staśto, Phys. Rev. D **56** (1997) 3991 [hep-ph/9703445].
- [34] P. Aurenche, R. Basu, M. Fontannaz and R. M. Godbole, “*An NLO calculation of the electroproduction of large- E_T hadrons*” [hep-ph/0312359];
M. Fontannaz, private communication.
- [35] A. D. Martin, R. G. Roberts, W. J. Stirling and R. S. Thorne, Eur. Phys. J. **C 23** (2002) 347.
- [36] I. Abt *et al.* [H1 Collaboration], Nucl. Instrum. Meth. **A 386** (1997) 310;
I. Abt *et al.* [H1 Collaboration], Nucl. Instrum. Meth. **A 386** (1997) 348.
- [37] B. Andrieu *et al.* [H1 Collaboration Calorimeter Group], Nucl. Instrum. Meth. **A 336** (1993) 499.
- [38] B. Andrieu *et al.* [H1 Collaboration Calorimeter Group], Nucl. Instrum. Meth. **A 350** (1994) 57.
- [39] T. Nicholls *et al.* [H1 Collaboration SPACAL Group], Nucl. Instrum. Meth. **A 374** (1996) 149.
- [40] R. D. Appuhn *et al.* [H1 Collaboration SPACAL Group], Nucl. Instrum. Meth. **A 382** (1996) 395.
- [41] A. A. Glazov, “*Measurement of the proton structure functions $F_2(x, Q^2)$ and $F_L(x, Q^2)$ with the H1 detector at HERA*”, Ph.D. Thesis, Berlin University, 1998, DESY-THESIS-1998-005.

- [42] T. Wengler, “*Measurement of π^0 -meson cross sections at low Bjorken- x in deep-inelastic $e p$ collisions at $\sqrt{s} = 300$ GeV,*” Ph.D. Thesis, Heidelberg University, 1999, DESY-THESIS-1999-011.
- [43] B. Andrieu *et al.* [H1 Calorimeter Group Collaboration], Nucl. Instrum. Meth. **A 344** (1994) 492.
- [44] J. Kwieciński, S. C. Lang and A. D. Martin, Phys. Rev. **D 55** (1997) 1273 [hep-ph/9608355].
- [45] R. Engel and J. Ranft, Phys. Rev. **D 54** (1996) 4244 [hep-ph/9509373].
- [46] C. Adloff *et al.* [H1 Collaboration], Z. Phys. **C 74** (1997) 221 [hep-ex/9702003].
- [47] A. Aktas *et al.* [H1 Collaboration], Eur. Phys. J. **C 33** (2004) 477 [hep-ex/0310019].
- [48] K. Konishi, A. Ukawa and G. Veneziano, Phys. Lett. **B 78** (1978) 243.

$x \cdot 10^4$	$(\frac{d\sigma_\pi}{dx})_{\pm tot}^{\pm stat}$ (nb)	$x \cdot 10^4$	$(\frac{d\sigma_\pi}{dx})_{\pm tot}^{\pm stat}$ (nb)
$2 < Q^2 < 4.5 \text{ GeV}^2$	$p_{T,\pi}^* > 2.5 \text{ GeV}$	$2 < Q^2 < 8 \text{ GeV}^2$	$p_{T,\pi}^* > 3.5 \text{ GeV}$
0.42—0.60	$990_{\pm 180}^{\pm 70}$	0.42—0.79	$410_{\pm 110}^{\pm 40}$
0.60—0.90	$1550_{\pm 250}^{\pm 80}$	0.79—1.1	$459_{\pm 80}^{\pm 36}$
0.90—1.4	$1010_{\pm 160}^{\pm 50}$	1.1—1.7	$375_{\pm 82}^{\pm 24}$
1.4—1.9	$770_{\pm 120}^{\pm 40}$	1.7—2.5	$284_{\pm 54}^{\pm 20}$
1.9—2.7	$503_{\pm 88}^{\pm 28}$	2.5—4.2	$110_{\pm 32}^{\pm 8}$
2.7—4.2	$141_{\pm 40}^{\pm 10}$		
$4.5 < Q^2 < 15 \text{ GeV}^2$	$p_{T,\pi}^* > 2.5 \text{ GeV}$	$8 < Q^2 < 20 \text{ GeV}^2$	$p_{T,\pi}^* > 3.5 \text{ GeV}$
1.1—1.8	$421_{\pm 71}^{\pm 23}$	1.1—2.0	$22_{\pm 11}^{\pm 5}$
1.8—2.5	$432_{\pm 67}^{\pm 24}$	2.0—2.9	$55_{\pm 14}^{\pm 7}$
2.5—3.5	$365_{\pm 55}^{\pm 19}$	2.9—3.9	$70_{\pm 17}^{\pm 8}$
3.5—4.8	$291_{\pm 43}^{\pm 15}$	3.9—5.5	$70_{\pm 16}^{\pm 7}$
4.8—6.8	$185_{\pm 32}^{\pm 10}$	5.5—11.0	$29.5_{\pm 6.4}^{\pm 2.1}$
6.8—11.0	$70_{\pm 12}^{\pm 4}$		
$15 < Q^2 < 70 \text{ GeV}^2$	$p_{T,\pi}^* > 2.5 \text{ GeV}$	$20 < Q^2 < 70 \text{ GeV}^2$	$p_{T,\pi}^* > 3.5 \text{ GeV}$
3.9—7.3	$79_{\pm 13}^{\pm 5}$	3.9—7.9	$16.6_{\pm 3.7}^{\pm 1.9}$
7.3—12.0	$78_{\pm 12}^{\pm 5}$	7.9—13.0	$14.5_{\pm 3.2}^{\pm 2.4}$
12.0—18.0	$50.3_{\pm 6.5}^{\pm 2.8}$	13.0—19.0	$12.4_{\pm 2.7}^{\pm 1.3}$
18.0—28.0	$27.1_{\pm 4.2}^{\pm 1.5}$	19.0—63.0	$3.60_{\pm 0.65}^{\pm 0.27}$
28.0—63.0	$5.1_{\pm 1.1}^{\pm 0.4}$		

Table 1: The inclusive π^0 -meson cross sections as shown in Figs. 2 and 3, presented together with the statistical and total uncertainties.

$p_{T,\pi}^*$	$(\frac{d\sigma_\pi}{dp_{T,\pi}^*})_{\pm tot}^{\pm stat}$ ($\frac{\text{pb}}{\text{GeV}}$)	$p_{T,\pi}^*$	$(\frac{d\sigma_\pi}{dp_{T,\pi}^*})_{\pm tot}^{\pm stat}$ ($\frac{\text{pb}}{\text{GeV}}$)	$p_{T,\pi}^*$	$(\frac{d\sigma_\pi}{dp_{T,\pi}^*})_{\pm tot}^{\pm stat}$ ($\frac{\text{pb}}{\text{GeV}}$)
$2 < Q^2 < 4.5 \text{ GeV}^2$		$4.5 < Q^2 < 15 \text{ GeV}^2$		$15 < Q^2 < 70 \text{ GeV}^2$	
2.5—2.8	$215_{\pm 36}^{\pm 9}$	2.5—2.8	$200_{\pm 34}^{\pm 8}$	2.5—2.9	$118_{\pm 18}^{\pm 5}$
2.8—3.3	$146_{\pm 27}^{\pm 6}$	2.8—3.4	$122_{\pm 21}^{\pm 5}$	2.9—3.5	$69.1_{\pm 8.8}^{\pm 3.3}$
3.3—4.0	$60.0_{\pm 14}^{\pm 3}$	3.4—4.1	$58_{\pm 11}^{\pm 3}$	3.5—4.7	$27.7_{\pm 4.7}^{\pm 2.0}$
4.0—5.2	$21.7_{\pm 4.7}^{\pm 1.4}$	4.1—5.2	$23.0_{\pm 4.9}^{\pm 1.5}$	4.7—8.0	$5.41_{\pm 0.96}^{\pm 0.38}$
5.2—8.0	$4.37_{\pm 0.83}^{\pm 0.38}$	5.2—8.0	$5.8_{\pm 1.2}^{\pm 0.4}$	8.0—15.0	$0.21_{\pm 0.06}^{\pm 0.04}$
8.0—15.0	$0.29_{\pm 0.26}^{\pm 0.06}$	8.0—15.0	$0.31_{\pm 0.12}^{\pm 0.06}$		

Table 2: The inclusive π^0 -meson cross sections as shown in Fig. 4, presented together with the statistical and total uncertainties.

x_π	$(\frac{d\sigma_\pi}{dx_\pi})_{\pm tot}^{\pm stat}$ (nb)		
$p_{T,\pi}^* > 2.5$ GeV			
	$0.000042 < x < 0.0002$	$0.0002 < x < 0.001$	$0.001 < x < 0.0063$
0.01—0.035	$7.2^{+0.2}_{\pm 1.0}$	$9.1^{+0.2}_{\pm 1.5}$	$3.44^{+0.12}_{\pm 0.48}$
0.035—0.04	$2.60^{+0.23}_{\pm 0.88}$	$3.87^{+0.27}_{\pm 0.81}$	$1.07^{+0.13}_{\pm 0.41}$
0.04—0.055	$0.85^{+0.07}_{\pm 0.23}$	$1.10^{+0.08}_{\pm 0.30}$	$0.44^{+0.05}_{\pm 0.10}$
0.055—0.075	$0.22^{+0.03}_{\pm 0.06}$	$0.28^{+0.03}_{\pm 0.09}$	$0.08^{+0.01}_{\pm 0.03}$
$p_{T,\pi}^* > 2.5$ GeV			
	$2 < Q^2 < 4.5$ GeV ²	$4.5 < Q^2 < 15$ GeV ²	$15 < Q^2 < 70$ GeV ²
0.01—0.035	$7.5^{+0.2}_{\pm 1.2}$	$7.3^{+0.2}_{\pm 1.1}$	$5.01^{+0.16}_{\pm 0.74}$
0.035—0.04	$3.32^{+0.28}_{\pm 0.92}$	$2.78^{+0.23}_{\pm 0.78}$	$1.51^{+0.14}_{\pm 0.39}$
0.04—0.055	$0.91^{+0.07}_{\pm 0.21}$	$0.89^{+0.07}_{\pm 0.22}$	$0.59^{+0.05}_{\pm 0.12}$
0.055—0.075	$0.22^{+0.03}_{\pm 0.08}$	$0.25^{+0.03}_{\pm 0.07}$	$0.12^{+0.02}_{\pm 0.03}$

Table 3: The inclusive π° -meson cross sections as shown in Figs. 5 and 6, presented together with the statistical and total uncertainties.

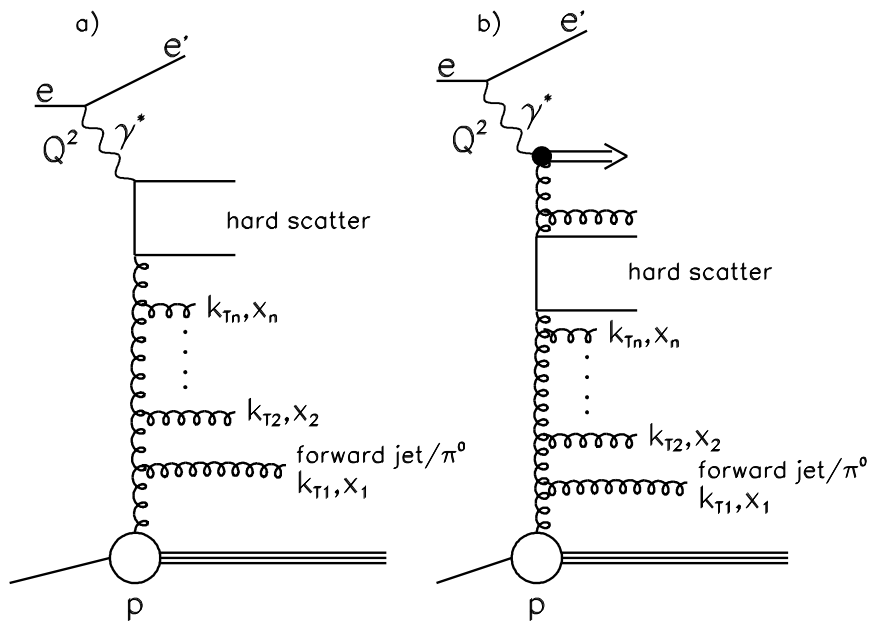


Figure 1: Generic diagrams for DIS processes at small x . The gluon longitudinal momentum fractions and transverse momenta are labelled x_i and k_{Ti} , respectively. (a) A gluon ladder evolves between the quark box, attached to the virtual photon, and the proton. (b) The partonic structure of the photon is “resolved”.

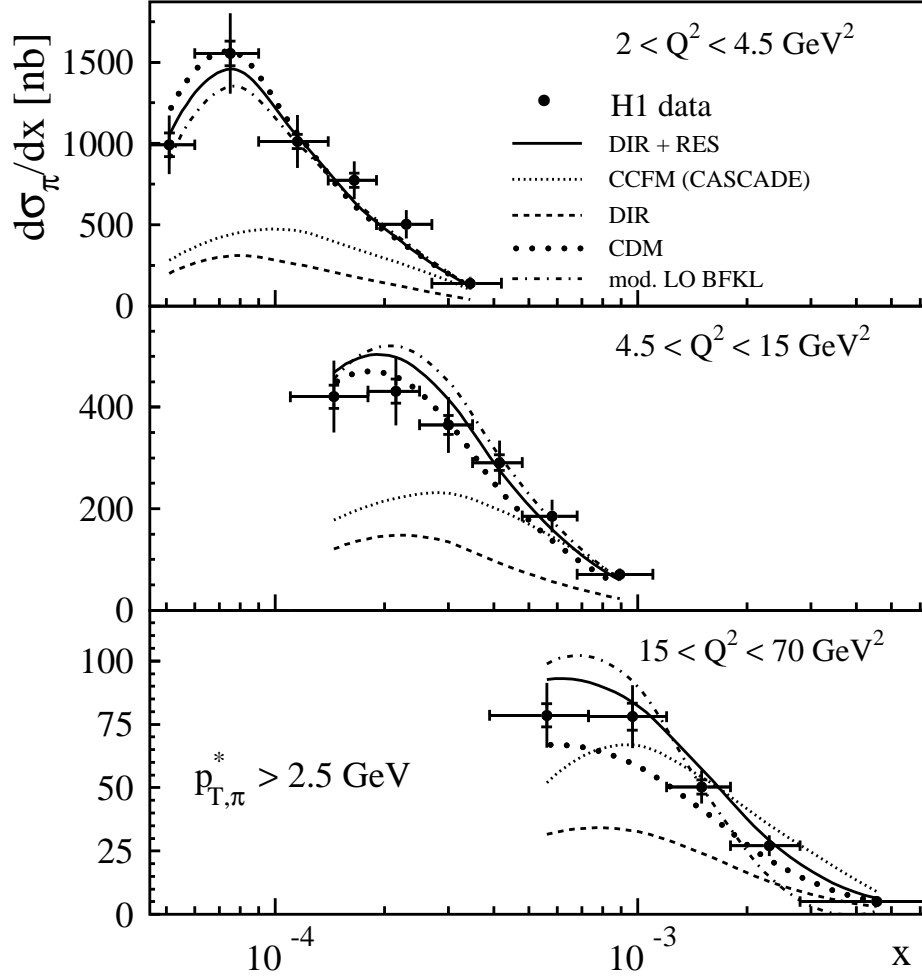


Figure 2: The inclusive ep cross section for forward π° mesons produced in the range $p_{T,\pi}^* > 2.5$ GeV, $5^\circ < \theta_\pi < 25^\circ$ and $x_\pi = E_\pi/E_p > 0.01$ as a function of Bjorken- x in three intervals of Q^2 . The DIS kinematic region is further specified by $0.1 < y < 0.6$. The inner error bars denote the statistical uncertainties and the outer error bars show the statistical and systematic uncertainties added quadratically. The predictions of five QCD-based models discussed in the text are shown.

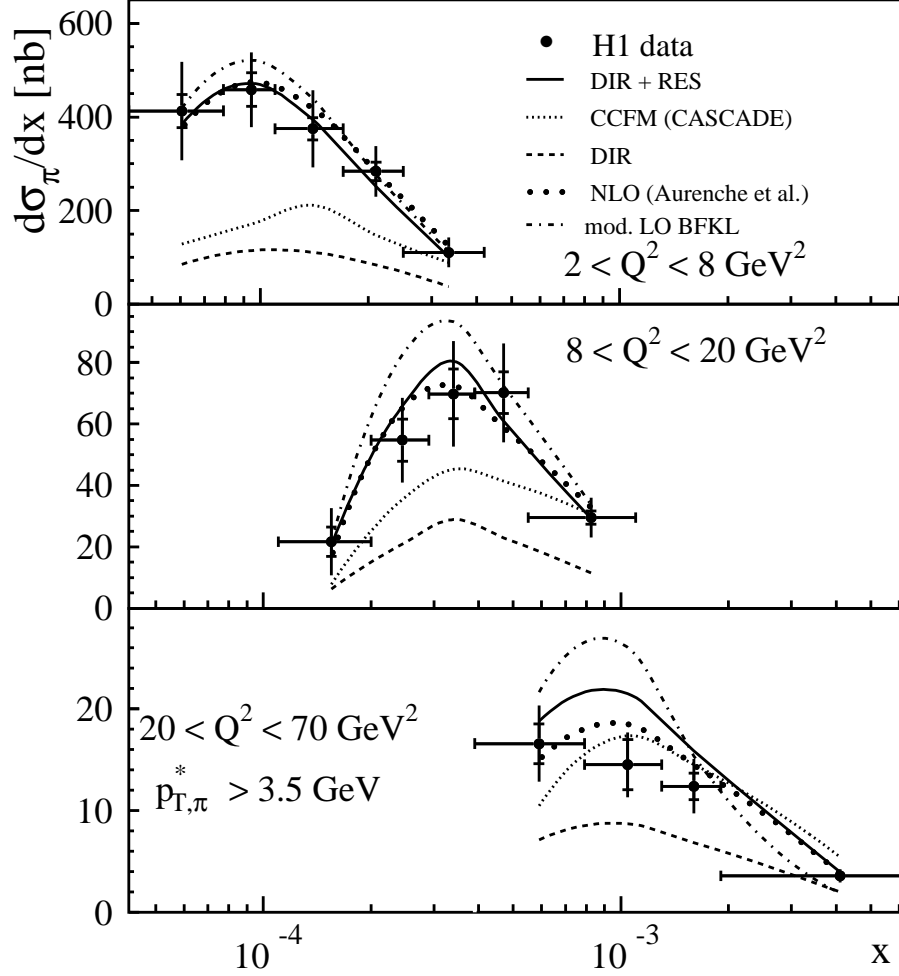


Figure 3: The inclusive ep cross section for forward π° mesons produced in the range $p_{T,\pi}^* > 3.5$ GeV, $5^\circ < \theta_\pi < 25^\circ$ and $x_\pi = E_\pi/E_p > 0.01$ as a function of Bjorken- x in three intervals of Q^2 . The DIS kinematic region is further specified by $0.1 < y < 0.6$. The inner error bars denote the statistical uncertainties and the outer error bars show the statistical and systematic uncertainties added quadratically. The predictions of five QCD-based models discussed in the text are shown.

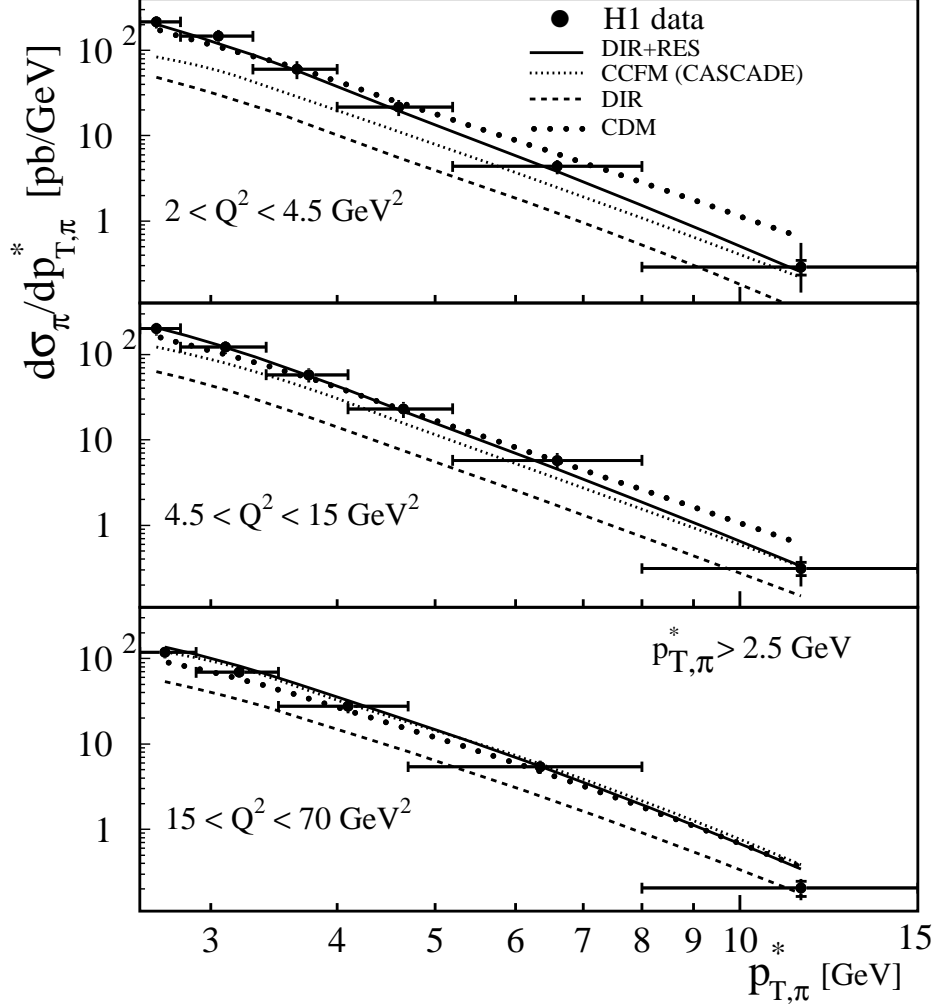


Figure 4: The inclusive ep cross section for forward π° mesons produced in the range $p_{T,\pi}^* > 2.5$ GeV, $5^\circ < \theta_\pi < 25^\circ$ and $x_\pi = E_\pi/E_p > 0.01$ as a function of $p_{T,\pi}$ in three intervals of Q^2 . The DIS kinematic region is further specified by $0.1 < y < 0.6$. The inner error bars denote the statistical uncertainties and the outer error bars show the statistical and systematic uncertainties added quadratically. The predictions of four QCD-based models discussed in the text are shown.

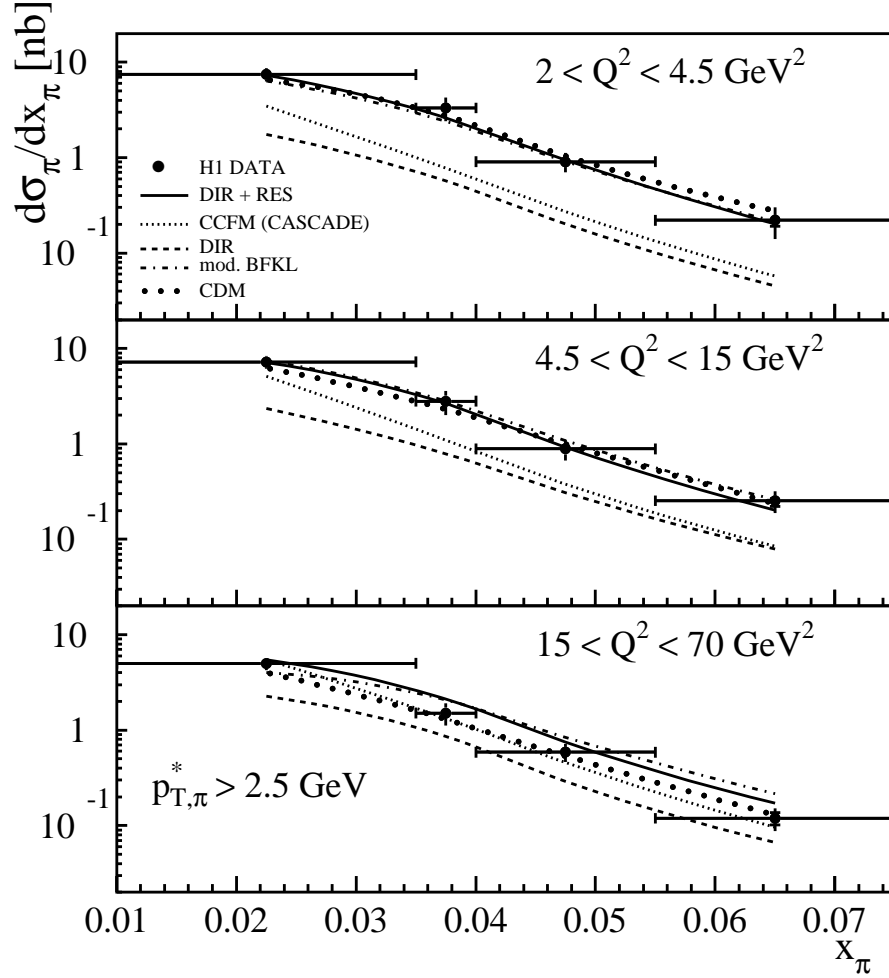


Figure 5: The inclusive ep cross section for forward π° mesons produced in the range $p_{T,\pi}^* > 2.5$ GeV, $5^\circ < \theta_\pi < 25^\circ$ as a function of x_π in three intervals of Q^2 . The DIS kinematic region is further specified by $0.1 < y < 0.6$. The inner error bars denote the statistical uncertainties and the outer error bars show the statistical and systematic uncertainties added quadratically. The predictions of five QCD-based models discussed in the text are shown.

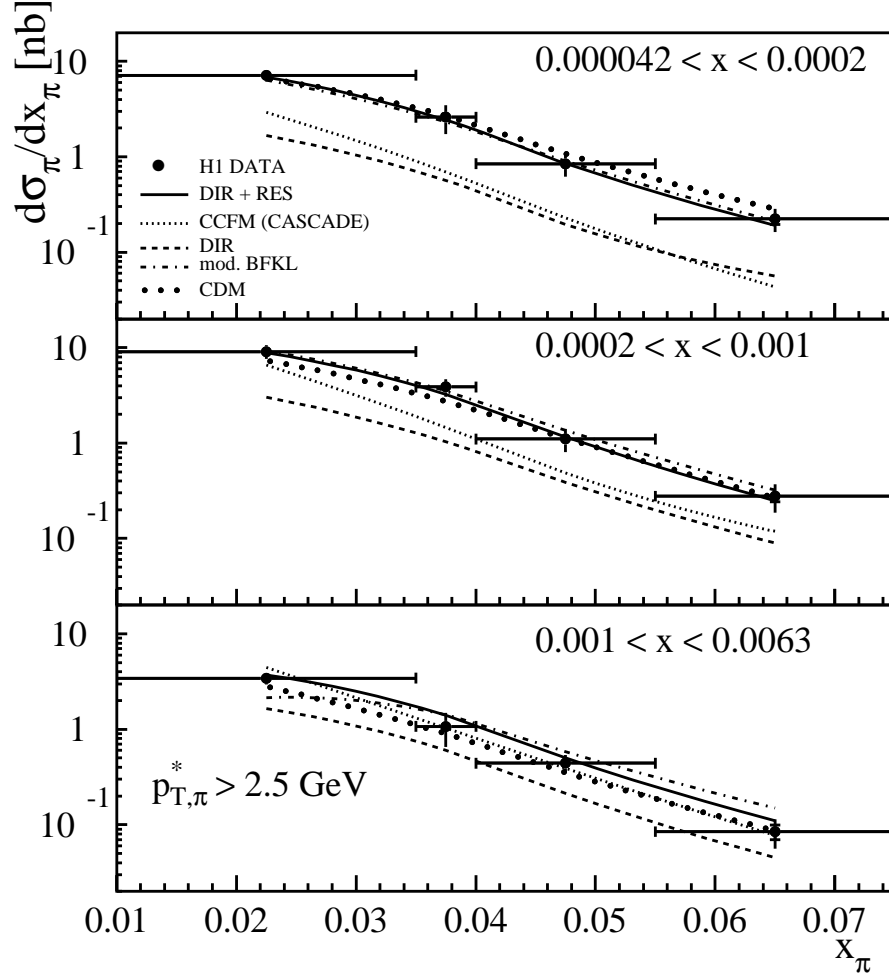


Figure 6: The inclusive ep cross section for forward π° mesons produced in the range $p_{T,\pi}^* > 2.5$ GeV and $5^\circ < \theta_\pi < 25^\circ$ as a function of x_π in three intervals of Bjorken- x . The DIS kinematic region is further specified by $2 < Q^2 < 70$ GeV² and $0.1 < y < 0.6$. The inner error bars denote the statistical uncertainties and the outer error bars show the statistical and systematic uncertainties added quadratically. The predictions of five QCD-based models discussed in the text are shown.

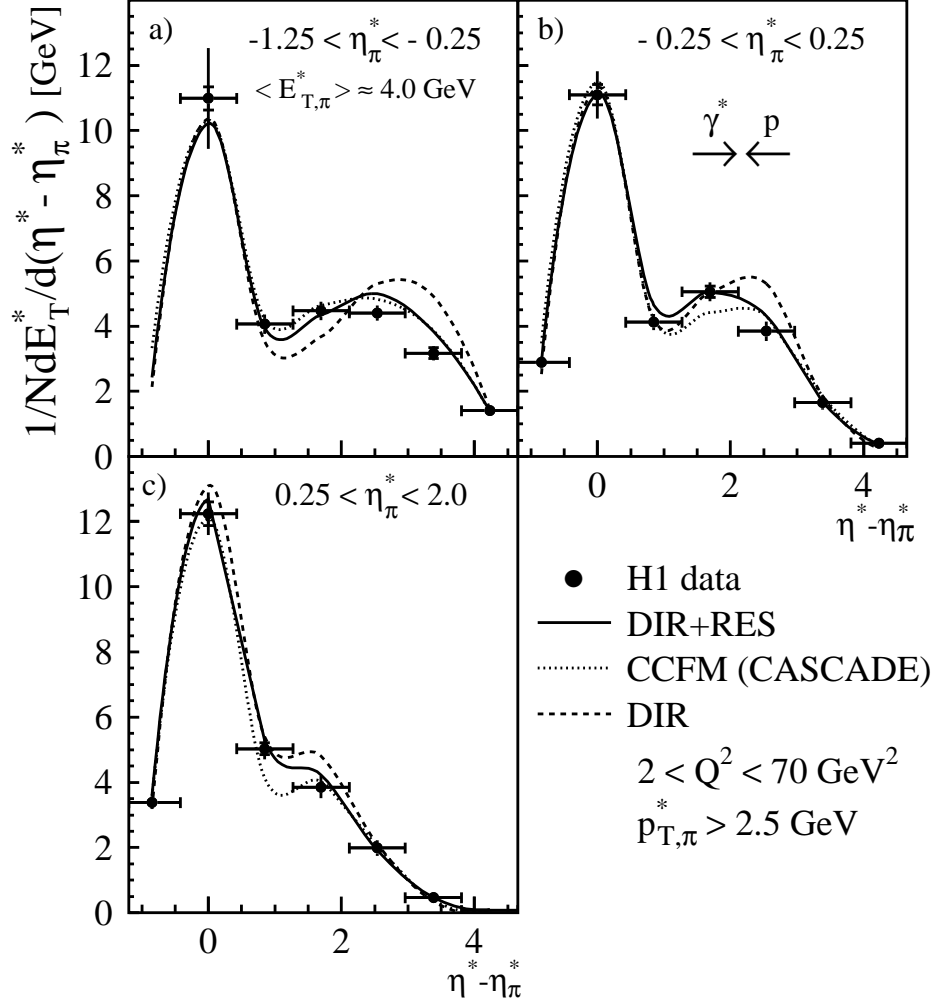


Figure 7: Distributions of transverse energy flow in events containing a forward π^0 produced in the range $p_{T,\pi}^* > 2.5$ GeV, $5^\circ < \theta_\pi < 25^\circ$ and $x_\pi = E_\pi/E_p > 0.01$. The transverse energy flow is presented as a function of the distance in pseudorapidity from the selected forward π^0 for various ranges in the π^0 pseudorapidity. The DIS kinematic region is specified by $2 < Q^2 < 70$ GeV² and $0.1 < y < 0.6$. The inner error bars denote the statistical uncertainties and the outer error bars show the statistical and systematic uncertainties added quadratically. The predictions of three QCD-based models discussed in the text are shown.

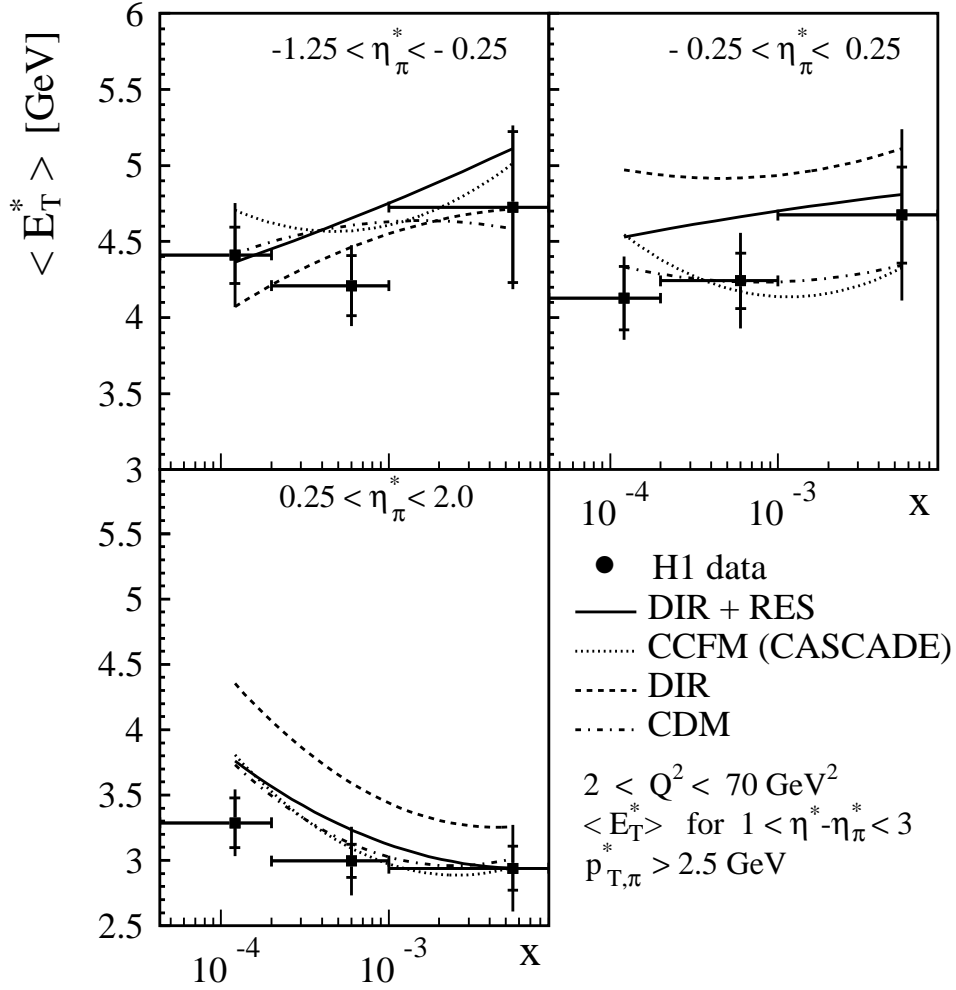


Figure 8: The mean transverse energy in events containing a forward π° produced in the range $p_{T,\pi}^* > 2.5 \text{ GeV}$, $5^\circ < \theta_\pi < 25^\circ$ and $x_\pi = E_\pi/E_p > 0.01$. The transverse energy is measured over the region $1.0 < \eta^* - \eta_\pi^* < 3.0$ as a function of Bjorken- x for three intervals of π° pseudorapidity. The DIS kinematic region is further specified by $2 < Q^2 < 70 \text{ GeV}^2$ and $0.1 < y < 0.6$. The inner error bars denote the statistical uncertainties and the outer error bars show the statistical and systematic uncertainties added quadratically. The predictions of four QCD-based models discussed in the text are shown.